ELSEVIER

Journal of Volcanology and Geothermal Research 101 (2000) 155–169

Journal of volcanology and geothermal research

www.elsevier.nl/locate/jvolgeores

Moment tensor analysis of near-field broadband waveforms observed at Aso Volcano, Japan

D. Legrand[a], S. Kaneshima[b], H. Kawakatsu[a,*]

[a]*Earthquake Research Institute, University of Tokyo, 1-1-1 Yayoi, Bunkyo-ku, Tokyo 113, Japan*
[b]*Department of Earth and Planetary Sciences, Faculty of Sciences, Tokyo Institute of Technology, O-Okayama, Meguro-ku, Tokyo, Japan*

Received 31 August 1998; received in revised form 27 February 1999; accepted 1 August 1999

Abstract

Locations and focal mechanisms of long-period volcanic events observed at Aso volcano, Japan, are determined by waveform inversion. Near-field broadband three-component seismograms of four to seven stations are simultaneously inverted in the time domain in order to find the six-component seismic moment tensor. A linear inversion is performed at each point of a 3D grid located under the volcano in order to constrain the centroid position and the focal mechanism of the source. The complete displacements, including near-field waves, in a homogeneous half-space for a general point source are taken into account. Inversions of 43 long-period tremors and six phreatic eruptions exhibit mainly an isotropic mechanism, with a minor deviatoric component that may originate from a north–south-trending crack. These events are all located in a small region at about 1.3 km depth beneath the active crater. The high accuracy, both of locations (a few hundred meters) and of focal mechanisms given by the inversion, is partly attributed to the rapid variation of the amplitude of the static displacement seen in the long-period part of the near-field seismograms. © 2000 Elsevier Science B.V. All rights reserved.

Keywords: waveform inversion; seismic moment tensor; isotropic component; volcanic tremor; near-field waves; broadband seismometers; crack

1. Introduction

Short-period seismometers have historically dominated in the monitoring of active volcanoes; however, broadband seismometers have been used recently to understand the physical processes of several volcanoes (e.g. Kawakatsu et al., 1992; Neuberg et al., 1994; Kaneshima et al., 1996; Ohminato and Ereditato, 1997; Ohminato et al., 1998; Rowe et al., 1998; Kawakatsu et al., 2000 – this issue). These authors show the presence of unusually long-period signals that cannot be observed by conventional short-period seismometers. One of the advantages of observing such long-period seismic signals is that we can easily analyze the waveforms to infer the physical processes occurring in the volcanoes (e.g. Kanamori and Given, 1981; Uhira and Takeo, 1994).

It is important to know the force systems or the focal mechanisms responsible for volcanic seismic signals. Different techniques have been used to find the focal mechanisms and/or locations of local earthquakes. Waveform inversions of near-field volcanic events recorded by a single broadband station have been used to retrieve the focal mechanism (e.g. Legrand, 1995). Focal mechanisms of volcanic events are conventionally determined by the use of polarities

* Corresponding author. Tel.: + 81-3-3812-2111, ext. 5700; fax: + 81-3-3812-9417.
E-mail address: hitosi@eri.u-tokyo.ac.jp (H. Kawakatsu).

0377-0273/00/$ - see front matter © 2000 Elsevier Science B.V. All rights reserved.
PII: S0377-0273(00)00167-0

of P-waves and/or polarization of S-waves (e.g. Foulger and Long, 1984; Julian and Foulger, 1996), or by waveform modeling of far-field waves (Julian and Sipkin, 1985). Locations are usually performed by the use of arrival times of P- and S-waves. Such conventional methods to determine both focal mechanisms and locations cannot be easily applied for volcanic tremors, because the first arrivals are not clear and S-waves generally cannot be identified. Others techniques such as relative locations of multiplets by cross-spectral methods may alternatively be used (e.g. Poupinet et al., 1982; Frémont and Malone, 1987; Lesage and Surono, 1995).

We present here a technique to jointly locate and find focal mechanisms for volcanic tremors and phreatic eruptions observed at Aso Volcano. The focal mechanisms are found by a linear waveform inversion in the time domain of the whole seismograms (near-field and far-field waves) performed at each grid point of a specified region below the crater. The locations are found by a systematic search of the best point-source focal mechanism in the region.

We show that the use of the filtered static displacements (hereafter noted as FSD) recorded in the near-field improves the accuracy of location because of the rapid spatial variations of their amplitudes, even for data filtered at long periods (15 and 7.5 s).

2. Data

We analyze the broadband seismic data collected by the Aso94 campaign (Kawakatsu et al., 2000 – this issue). For details of the observed data, readers are referred to this paper. At Aso Volcano, Kyushu, volcanic signals with very long periods (longer than 7 s) and with rather short durations (several tens of seconds) have been observed (e.g. Sassa, 1935; Kawakatsu et al., 1994). They are called long-period tremors (LPTs) by Kaneshima et al. (1996). We use "long-period" for periods substantially longer than 1 s; note that this convention is different from those based on recordings of short-period seismometers (e.g. Chouet, 1996). The spectrum of such LPTs stacked over 1 day shows generally four dominant peaks at 15, 7.5, 5 and 3 s (Kaneshima et al., 1996; Kawakatsu et al., 2000 – this issue). For several years, LPTs have been emitted continually by the volcano even when there is no surface activity. Examples of LPT and a phreatic eruption are shown in Fig. 1. We locate such LPTs and phreatic eruptions using data from up to seven broadband stations and determine their focal mechanisms at the same time. The most energetic period of 15 s is always clearly recorded, because it is out of the range of frequencies of the microseisms. The events filtered at the 7.5 s period are inverted only when the signals at this period are clear enough (e.g. September 1994).

3. Waveform modeling

3.1. Determination of location and focal mechanism by waveform inversion

Waveforms emitted from a point source may be described as follows (e.g. Aki and Richards, 1980):

$$u_i(\mathbf{x}, t) = M_{jk}(\boldsymbol{\xi}, t) * g_{ij,k}(\boldsymbol{\xi}, 0; \mathbf{x}, t) \quad (1)$$

where **u**, **M** and **g** are the displacement, the seismic moment tensor and Green's functions tensor, respectively. The asterisk $*$ represents the temporal convolution and **x** and $\boldsymbol{\xi}$ the locations of the receiver and seismic source, respectively.

The observed shapes of LPTs are almost identical at all the components of all the stations (Figs. 3 and 4), indicating that these near-field recordings at long periods have little sensitivity to the spatial variation of the moment release at the source and are mainly proportional to the source time function (discussed in more detail in Section 4). We therefore select one of these components to represent the source time function (north component of KHE station). We further assume a homologous source time function $f(t)$, i.e. the seismic moment tensor can be expressed as $M_{jk}(\boldsymbol{\xi}, t) = M_{jk}(\boldsymbol{\xi})f(t)$. Hence, the waveform fitting is achieved mainly by modeling the relative amplitude of the source time function (or the FSD), rather than the shape of the waves.

A linear inversion of displacement has been performed in the time domain at each point of a 3D grid ($800 \times 800 \times 800$ m^3 sampled each 100 m) under the crater in order to find the seismic moment tensor. The corresponding RMS errors between data and

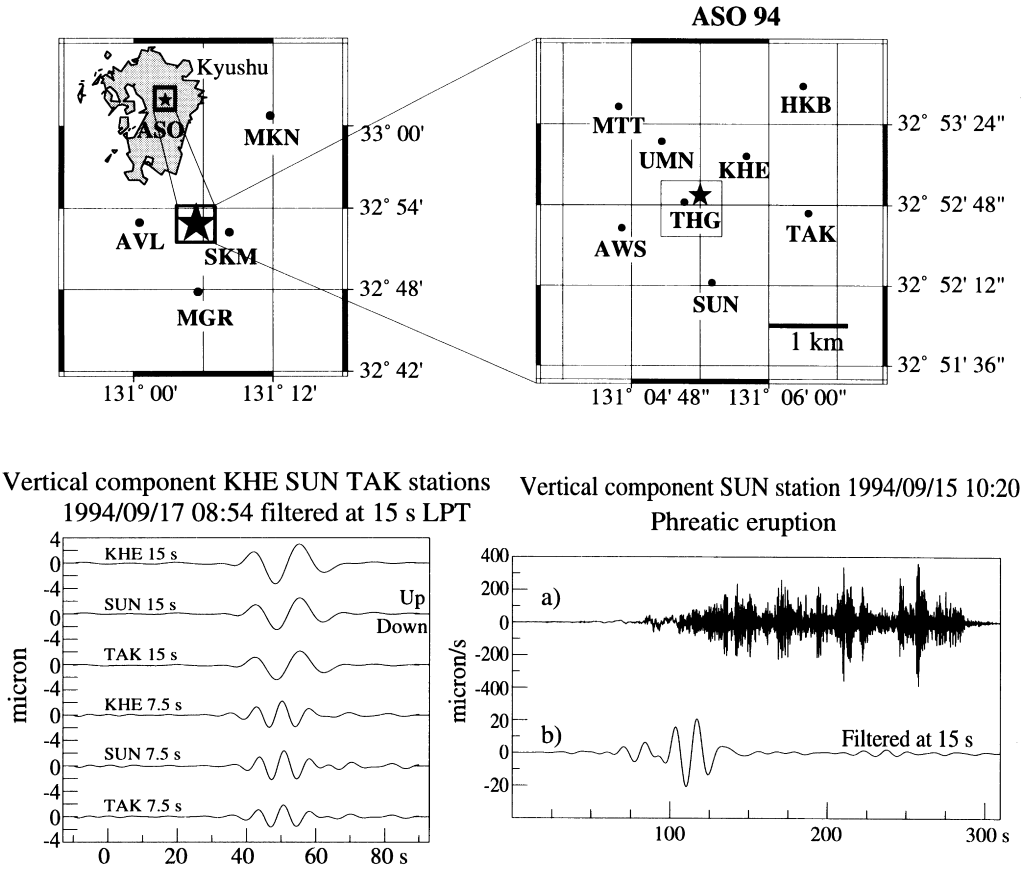

Fig. 1. Summary of the Aso94 campaign (Kawakatsu et al., 2000 – this issue). Top: locations of the broadband seismic stations around Aso, Kyushu. The star represents the position of the active crater. The altitude of the active crater (1.16 km) is taken as reference for the depths calculated in this study. Top right: the square around the first crater corresponds to the region where the 3D grid inversion is performed. Bottom left: example of vertical component seismograms of long-period tremor recorded at three stations (KHE, SUN and TAK) band-pass filtered around 15 and 7.5 s. Bottom right: example of vertical velocity component seismogram of a phreatic eruption (94/09/15 at 10:20 GMT) recorded at station SUN. (a) raw record, (b) filtered between 10 and 30 s (hereafter called 15 s period for the sake of rapidity).

synthetics are calculated by:

$$\text{RMS error} = \frac{1}{N^{1/2}} \frac{\left\{\sum_{i=1}^{3N} \int (O_i(t) - C_i(t))^2 \, dt\right\}^{1/2}}{\left\{\sum_{i=1}^{3N} \int (O_i(t))^2 \, dt\right\}^{1/2}} \quad (2)$$

where N is the number of stations, and $O_i(t)$ and $C_i(t)$ denote observed and calculated waveforms, respectively. The best location corresponds to the point of the grid with the smallest RMS error, and the associated seismic moment tensor corresponds to the best focal mechanism.

For the Green's functions, we used a simple homogeneous half-space model for which the exact expressions of the complete displacement field, i.e. the near-field waves and the far-field waves, are calculated in the time domain (Johnson, 1974). These Green's functions are calculated only one time for each point of the grid and each station, are stored in memory, and are used for the inversion of all the events. The correction for the station altitude is made as follows: each station is assumed to be at the free surface of the half space, and the relative elevation of the station to the source is equated to the depth of the source in the half space. The relative distance between a source and a station is used to calculate Green's functions for each station.

The altitude of reference is 1.16 km, and corresponds to the surface of the crater lake represented by a star in Fig. 1. We justify the use of this simple model on the grounds of wavelength of the signals considered. With an assumed V_P of 1.5 km/s and V_S of 0.8 km/s (Matsubayashi, 1995), source size of no more than several hundred meters (Kaneshima et al., 1996) and dominant periods of 15 and 7.5 s, the wavelengths will be on the order of 20 km and should be relatively unaffected by small-scale heterogeneities of the unknown structure, permitting the use of a simple half-space model and an assumed point source.

3.2. Results of inversions

We analyzed the data recorded in September and November of 1994 when several phreatic eruptions as well as many LPTs were observed. We inverted six phreatic eruptions and 43 LPTs. Temporary stations (UMN and THG, Fig. 1) were installed in November 1994 for a duration of about 2 weeks. During this period, seven nearby stations were available (THG, AWS, SUN, UMN, KHE, TAK and HKB, Fig. 1). Records from up to these seven broadband stations are used for the inversion. Records of five other stations (MTT, SKM, AVL, MGR and MKN) are used (when available) to check the quality of the obtained seismic moment tensor. They are not used in the inversion because of the lower quality of the signals. The lack of precise knowledge of the seismic velocity structure between the crater and these stations also hampers incorporating their seismograms in the inversion.

3.2.1. LPTs at 15 s

Figs. 2 and 3 show the results of inversions for a typical LPT (94/11/23, at 07:25 GMT) inverted with seven stations filtered between 10 and 30 s (hereafter called 15 s for the sake of rapidity). The best seismic moment tensor of the LPT shown in Fig. 2 is listed in Table 1. The focal mechanism found by the inversion plotted in Fig. 2 is mainly isotropic (97%, cf. Appendix A). Fig. 3 shows the corresponding seismograms.

3.2.2. Phreatic eruptions at 15 s

Fig. 4 shows the results of inversions for a phreatic eruption (94/09/15, at 10:20 GMT) using displacement seismograms low-pass filtered at 15 s. The amplitude of that eruption is about 10 times bigger than the amplitude of a typical LPT, and the signal-to-noise ratio is correspondingly larger. The best seismic moment tensor is listed in Table 1. The focal mechanism is again mainly isotropic (98%, cf. Appendix A). Compared to LPTs, the spectra of phreatic eruptions show rather broad continuous peaks. To demonstrate that the study is not highly dependent on the narrow filter we used for phreatic eruptions, we have inverted the event of Fig. 4 without applying any filter. The result of the waveform modeling is shown in Fig. 5, verifying the method for unfiltered data.

3.2.3. LPTs at 7.5 s

We inverted 17 LPTs (17 September 1994) around a period of 7.5 s, the second most energetic peak. At this period (7.5 s), the waveform fit is a little worse than that of the 15 s inversion. This is probably because both structure and source complexity are likely to affect the 7.5 s waves more they affect the

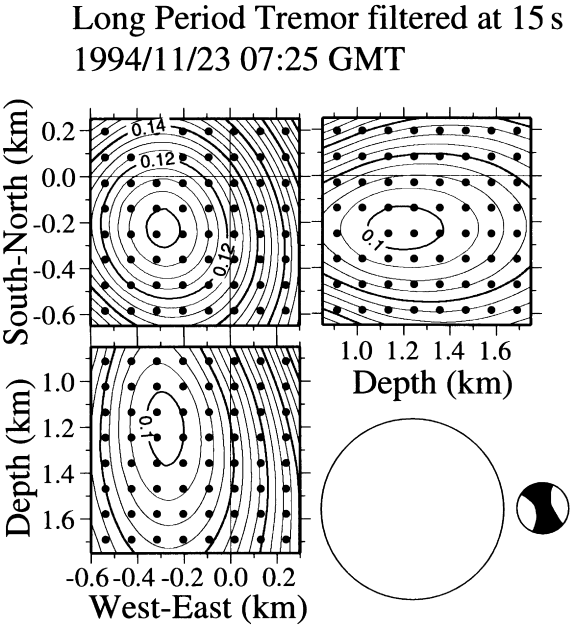

Fig. 2. Location of an LPT (94/11/23 at 07:25 GMT) filtered around 15 s. Contour plot of RMS errors projected onto three orthogonal planes which include the smallest RMS error corresponding to the best location. The corresponding seismic moment tensor is isotropic (97% of the total moment) with a small deviatoric part. The lower-hemisphere projections of the two components are shown in the relative size of the definition of Iso and Crack in Section 4.2.

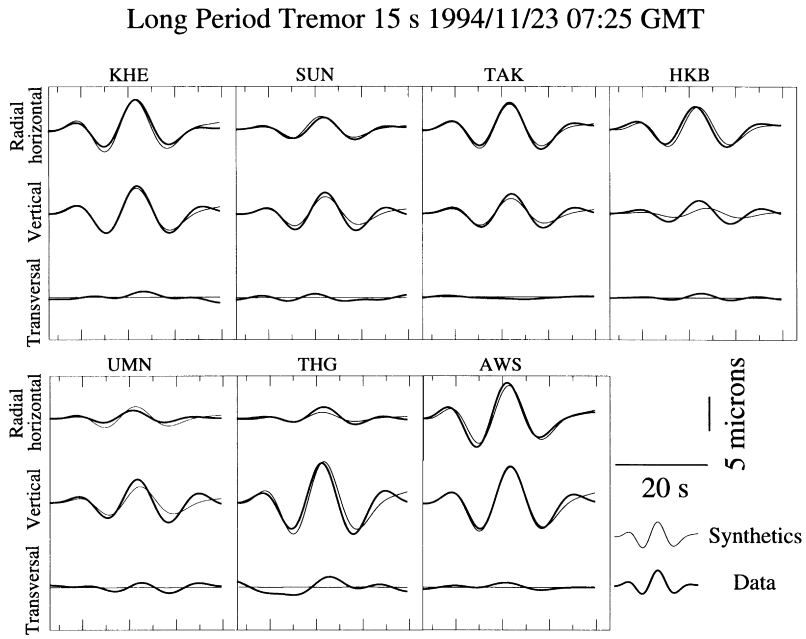

Fig. 3. Data (thick curves) and synthetics (thin curves) calculated from the result of inversion of the event of Fig. 2. The data are filtered displacements and expressed in microns.

Table 1
The best moment tensor solutions for LPTs (15 s), phreatic eruptions (15 s) and LPTs (7.5 s) are given (the left most solutions in Fig. A1). The error of each component is estimated from the standard deviation of the distribution of the component of all the solutions studied (there are 43, 6 and 17 of such solutions, respectively). In order to combine the information available in the moment tensors of different magnitude, the moment tensors are first normalized by the total seismic moment M_0^M (Appendix A). The scaled moment tensors are then used to estimate the standard deviation of each component, which is further scaled back to the value in the table using M_0^M of the best solutions. Corresponding eigenvalues and eigenvectors are given as North, East, Vertical. The eigenvalues of LPTs (15 s) suggest that the non-isotropic part corresponds mainly to a vertical crack in the direction of 15°NNW–SSE. Notations: $I = 1/3(M_{\theta\theta} + M_{\phi\phi} + M_{rr})$; $C = 1/3(M_{\theta\theta} + M_{\phi\phi} - 2M_{rr})$; $D = 1/2(M_{\theta\theta} - M_{\phi\phi})$

M_{ij}	LPT at 15 s (10^{11} N m)	Phreatic eruption at 15 s (10^{11} N m)	LPT at 7.5 s (10^{11} N m)
I	−3.54 ± 0.19	−63.82 ± 3.92	−2.04 ± 0.09
C	−0.24 ± 0.24	−3.38 ± 5.33	0.06 ± 0.11
D	0.67 ± 0.14	11.31 ± 2.52	0.41 ± 0.06
$M_{r\theta}$	0.01 ± 0.02	0.79 ± 1.28	0.12 ± 0.02
$M_{r\phi}$	−0.11 ± 0.03	−0.24 ± 0.28	0.13 ± 0.02
$M_{\theta\phi}$	0.39 ± 0.07	3.32 ± 1.15	0.11 ± 0.02

Eigenvalue	Eigenvector (North, East, Vertical)	Eigenvalue	Eigenvector (North, East, Vertical)	Eigenvalue	Eigenvector (North, East, Vertical)
−4.44	(0.257 0.962 −0.091)	−77.31	(0.143 0.990 −0.021)	−2.47	(0.080 0.944 0.321)
−3.29	(0.068 0.076 0.995)	−60.52	(−0.105 0.036 0.994)	−2.10	(−0.285 −0.287 0.914)
−2.88	(0.964 −0.261 0.045)	−53.64	(0.984 −0.140 0.110)	−1.55	(0.955 −0.165 0.246)

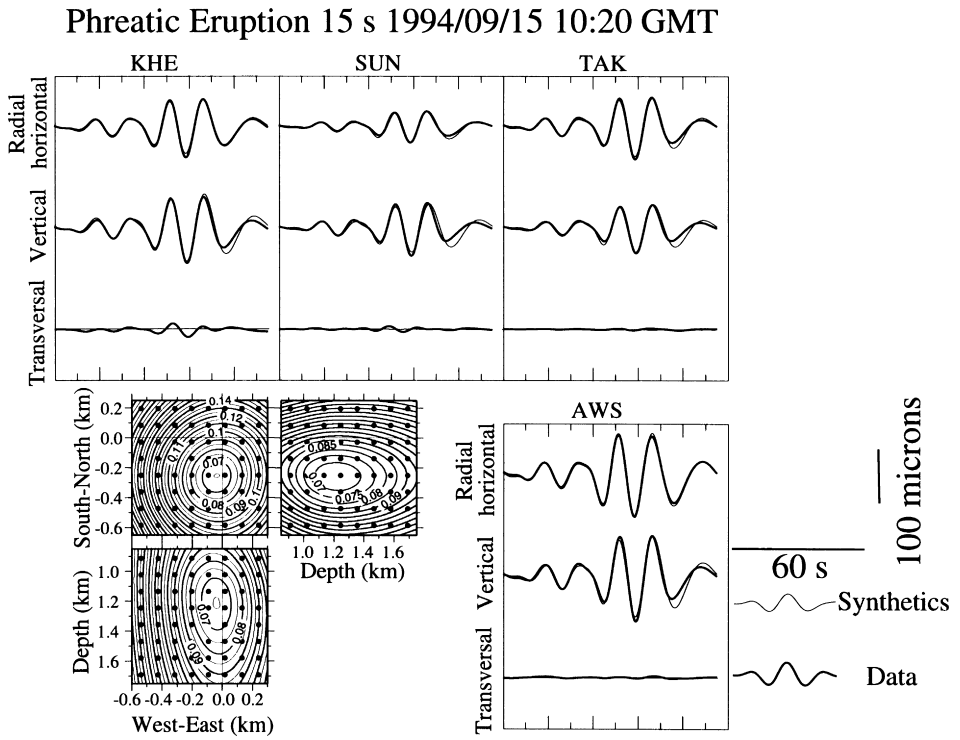

Fig. 4. Similar to Figs. 2 and 3 for a phreatic eruption of 94/09/15 at 10:20 GMT.

15 s waves. Fig. 6 shows the result of the inversion of the best LPT filtered around 7.5 s. At this period, all LPTs also have mainly isotropic mechanisms (cf. Appendix A).

Some examples of the best solutions of LPTs at periods of 15 and 7.5 s and phreatic eruptions at 15 s are represented in Appendix A. Solutions for the different events are very stable. The mechanisms are mainly isotropic, and all events have more than 84% of isotropic component. The isotropic part **I** is defined as $\mathbf{M} = \mathbf{I} + \mathbf{D}$, where **D** is the deviatoric part (i.e. $\mathrm{tr}(\mathbf{D}) = 0$). The deviatoric parts of the solutions of LPT at 15 s and phreatic eruption at 15 s show consistent patterns (Fig. A1(a) and (b)). The eigenvector associated with the largest absolute eigenvalue of the deviatoric part is very stable. A similar observation also holds for the solutions of LPT at 7.5 s (Fig. A1(c)), although the directions of the axes corresponding to the largest eigenvalues are perpendicular to those mentioned above. We tested the influence of the different number of stations used for the inversions on the solutions as follows. For those events for which data from the seven stations were available, inversions using only four or five stations data were performed. The solutions (both location and focal mechanism) of the inversion using fewer stations (four to five) are consistent with full (seven) station inversions. The primary source of difference in the seismic moment tensor is the poor constraint of the deviatoric part for noisy events. For phreatic eruptions with a large signal-to-noise ratio the deviatoric parts are generally stable.

3.2.4. Centroid locations

The RMS error contour plots in Figs. 2, 4 and 6 cover a cubic region with an 800 m-long side, represented by a small square in Fig. 1. The uncertainty of the location is about 100–200 m horizontally and about 200–400 m vertically for the events of Figs. 2 and 4. These values correspond to the region within which the RMS errors are no larger than 10% of the minimum value. The value 10% is chosen such that the gradient of the contour lines changes quickly around the value. The uncertainty is a little bigger

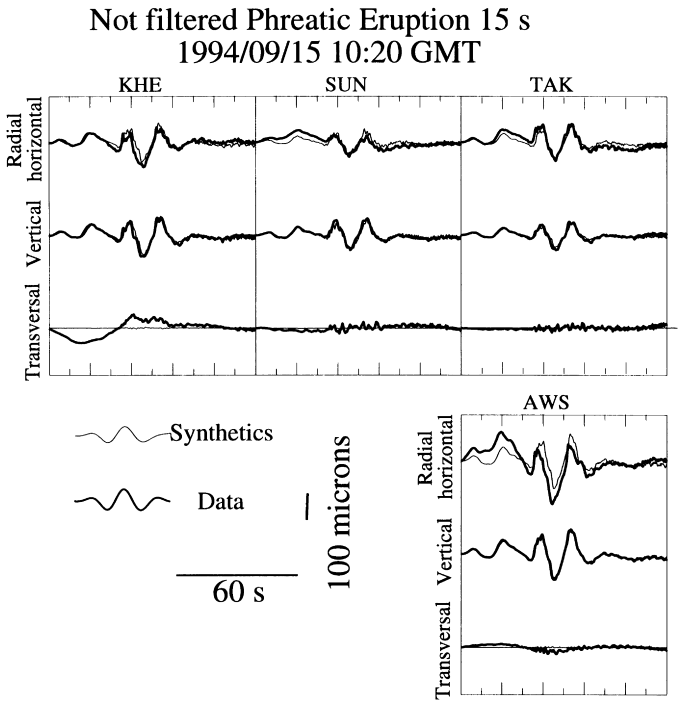

Fig. 5. Same event as in Fig. 4 for unfiltered displacements. The same source location is assumed for the inversion.

for noisier data, but never exceeds a few hundred meters.

The locations of all the solutions are shown in Fig. 7. Locations of the six phreatic eruptions around 15 s are concentrated 50 m east and about 250 m south of the first crater, at a depth around 1.1 km. Locations for the LPTs around 15 s are about 140 m west and 250 m south of the first crater, at a depth of 1.3 km. Locations for the LPTs around 7.5 s are about 70 m east and 360 m south of the first crater, and at 1.1 km depth (Table 2). These values are obtained as the mean of the events shown in Fig. 7. The 7.5 s-filtered LPTs seem to occur a little shallower than the 15 s ones, but we are in the limit of accuracy of location and we cannot claim here that this difference is significant. Locations of LPTs found by this grid search for both the 15 and 7.5 s data are similar to those found by directions of polarization (cf. Appendix B). They are also generally consistent with the location determined by the three-component semblance method introduced by Matsubayashi (1995) and Kawakatsu et al. (2000 – this issue), and by the Mogi deformation model for a buried sphere in a homogeneous half space (Mogi, 1958; Kaneshima et al., 1996).

3.3. Constraint of the isotropic and deviatoric parts

When the six components of the seismic moment tensor are used for a waveform inversion, it is important to check if all the components (especially the isotropic component) are well constrained. We invert both for a pure deviatoric seismic moment tensor (five parameters) and for a pure isotropic seismic moment tensor (one parameter). The RMS error for the event of Figs. 2 and 3 corresponding to the deviatoric part is 0.364, which is significantly larger than that for the pure isotropic model (0.173). In short, the one-parameter isotropic model better explains the data than the five-parameter deviatoric model. Hence, the isotropic component must contain a significant part of the total seismic moment tensor. The six-component seismic moment tensor, however, has a RMS error of 0.098, significantly smaller than the previous values, which compels a full moment tensor analysis.

Because of the same azimuthal independency of the

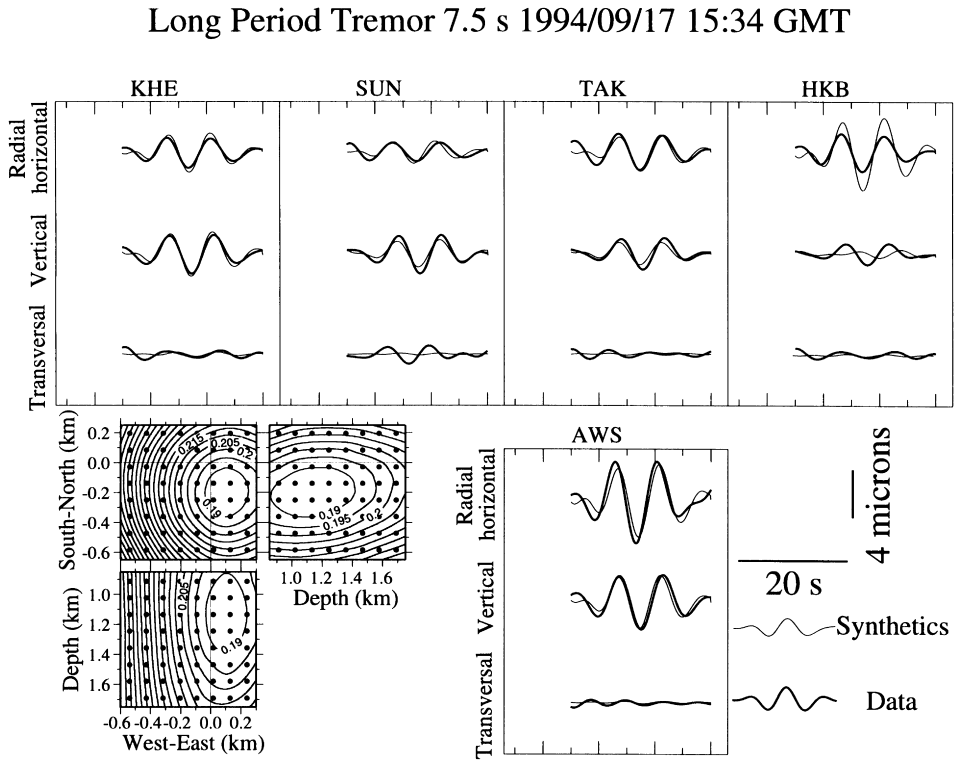

Fig. 6. Result of the best LPT filtered around 7.5 s of 94/9/17 at 15:34 GMT.

radiation amplitude, there is often a trade-off between $I = \frac{1}{3}(M_{rr} + M_{\theta\theta} + M_{\phi\phi})$ (the isotropic part) and $C = \frac{1}{3}(M_{\theta\theta} + M_{\phi\phi} - 2M_{rr})$ (the vertical CLVD part) (Knopoff and Randall, 1970) or M_{rr} and $M_{\theta\theta} + M_{\phi\phi}$ (e.g. Kawakatsu, 1996). In order to distinguish I and C, it is necessary to have stations at a variety of distances from the source. In our problem we could use data from five additional stations located further away from the crater (MTT, SKM, AVL, MGR and MKN of Fig. 1). We have inverted the seismograms for the four closer stations KHE, SUN, TAK and AWS available for the phreatic eruption of Fig. 4, and calculated synthetic seismograms for the other stations (when these stations are included, the quality of the solution of inversion is substantially aggravated, which may due to the lack of knowledge of the detailed structure). Fig. 8 compares the data and synthetics corresponding to the I and C components. Synthetic seismograms of I and C components are quite different for the radial horizontal component of HKB. They are negatively correlated for the vertical component of MTT and HKB and for the vertical and radial horizontal component of THG, AWS, SUN, UMN, KHE, TAK and positively correlated for the other components. So the use of both sets of data, (THG, AWS, SUN, UMN, KHE, TAK) and (MTT, HKB, SKM, AVL, MGR, MKN), should allow us to distinguish the I and C components. Comparing the data and synthetics as shown in Fig. 8, we conclude that the isotropic component, I, can explain the data whereas the vertical CLVD, C, cannot.

If we include the single-force component for the source description (e.g. Kanamori and Given, 1982), the situation becomes more complicated. The RMS error between the data and the seismograms calculated from a vertical single force source is 0.243, not so different from that (0.173) of a pure isotropic model. Based solely on the RMS error between data and synthetics, it appears difficult to distinguish a

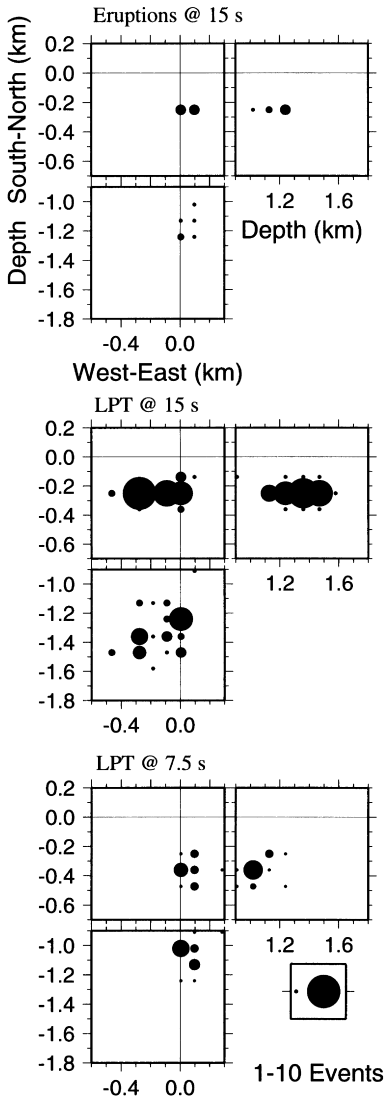

Fig. 7. Location of events corresponding to the point of the smallest RMS of the 3D grid (100 m sampled). The size of the circles is proportional to the number of events located at the grid point. The origin of the coordinate system corresponds to the active crater. Left: locations of the six phreatic eruptions around 15 s (September 1994). Middle: locations of the 43 LPTs around 15 s (September–November 1994). Right: locations of the 17 LPTs around 7.5 s (17 September, 1994).

single vertical force from an isotropic source; however, we believe that a single force component is unlikely to be significant, because no substantial material except gas, water and small rocks is emitted from the volcano.

4. Discussion

4.1. Long-period near-field seismograms and FSD

In the near-field, the near-field terms are predominant (e.g. Aki and Richards, 1980). These waves travel with a velocity between P- and S-waves velocities, and are very low frequency in nature. They are not simply linearly polarized, and contribute to the static displacement. To illustrate the nature of the near-field waveform data that we analyze, we show in Fig. 9 the synthetic displacement seismograms calculated for an isotropic source at a variety of distances for the radial component which corresponds to the direction of the station from the source. At stations close to the source (0.05 km, top of Fig. 9a), the seismogram resembles the source time function (0.2 s ramp function), whereas at more distant stations (20 km, bottom of Fig. 9a) the seismogram resembles the derivative of the source time function. Fig. 9b shows the synthetic seismograms for a source located at the depth of 1 km seen at different distances and at different frequencies. The amplitudes of 15 s filtered signals are larger for distances shorter than 5 km and again larger for distance greater than 10 km. This is due to the presence of near-field terms filtered at 15 s which decay rapidly for distances smaller than 5 km and due to the arrival of surface waves for distances larger than 10 km.

Amplitudes of synthetic seismograms shown in Fig. 9b are plotted in Fig. 10 as a function of the radial distance and frequency. Very near the source (Fig. 10a), the amplitudes of the band-pass filtered synthetic seismograms for different periods (15, 7.5, 1 and 0.5 s) decay with distance as $1/r^2$, exactly as static displacements are expected to do. In the very near field, we thus should observe static displacements (i.e. the source time function) for all frequencies listed above. Fig. 10b shows the case of intermediate distances for synthetics originating from a source at a depth of 1 km, corresponding to a typical modeled source depth at Aso Volcano. Within the radial distance of 5 km, which corresponds to the distance of our data used for inversions, the amplitudes of seismograms filtered at 15 and 7.5 s still decay as $1/r^2$, as the static displacements do. At shorter periods the decay rate is between $1/r^2$ and $1/r$, so that the waves are a mixture of near-field

Table 2
Locations found by the grid inversion. Depth is with respect to reference level situated at 1.16 km altitude (the top of the first crater)

Events	Period of study (s)	North direction (km)	East direction (km)	Depth (km)
LPTs	15	− 0.250 ± 0.2	− 0.140 ± 0.2	1.3 ± 0.4
Eruptions	15	− 0.250 ± 0.2	0.050 ± 0.2	1.1 ± 0.4
LPTs	7.5	− 0.360 ± 0.2	0.070 ± 0.2	1.1 ± 0.4

waves, static displacements and far-field waves. At large distances (Fig. 10c), the amplitudes of the filtered synthetic seismograms decay as $1/r$, as for far-field P- and S-waves, for all the periods tested (15, 7.5, 1 and 0.5 s).

We illustrate this effect on the actual data (Fig. 10d) for a phreatic eruption (crosses) and for a LPT (diamonds) at 15 s of period. At short distances, the waves decay as $1/r^2$, whereas at large distances the waves decay as $1/r$; the decay is between $1/r^2$ and $1/r$ for intermediate distances.

To summarize these observations shown in Fig. 10, the waveform data (both 15 and 7.5 s within 5 km from the crater) we analyzed in this paper mainly consist of the FSD. The waveforms resemble the source time function. By the inversion, we effectively invert the spatial variation of the amplitude of the FSD. Although the differences in travel time from

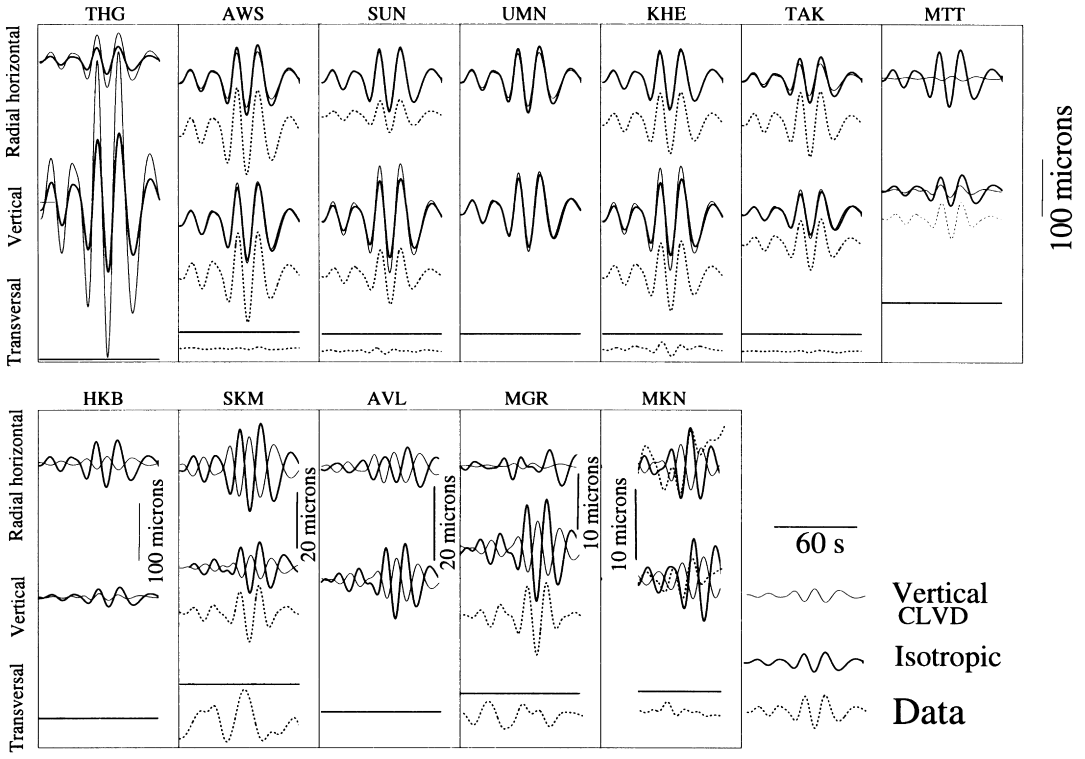

Fig. 8. Comparison of synthetics and data for all stations of event of Fig. 4. Synthetic seismograms corresponding to an isotropic source (thick solid line) and a vertical CLVD (thin solid line) are shown. They are scaled such that the radial horizontal components at KHE have identical amplitude. As the data (dotted line) fit better with the component I (isotropic), and not with the component C (vertical CLVD), the source is mainly isotropic (see text).

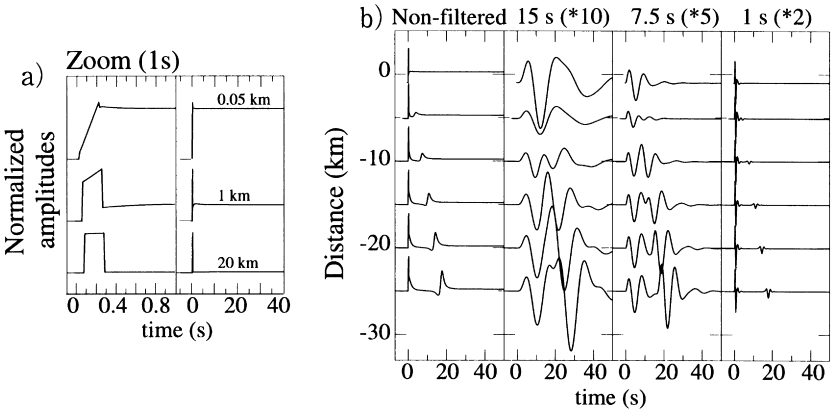

Fig. 9. (a) Synthetic seismograms for a homogeneous half-space of the radial component for three source depths: 0.05, 1 and 20 km (for stations situated right above the source). The radial direction here is defined as the direction of the receiver from the source (i.e. synthetics are actually for the vertical component in this plot). The synthetics on the left columns are enlarged versions of the corresponding ones on the right column. The source time function is a ramp with a rise time of 0.2 s. (b) Comparison of synthetic seismograms seen at different frequencies and different distances. The distance here is the radial distance, i.e. source–receiver distance. Radial component seismograms for an isotropic source located at a depth of 1 km are shown. Plotted from left to right; unfiltered, band-pass filtered around 15, 7.5 and 1 s. In each column, signals are normalized by a $1/r$ factor. The filtered signals are further multiplied by a constant factor given in the parenthesis on the top of each column. Note that the short-period signals in unfiltered and 1 s synthetics exhibit nearly constant amplitude at all distances, suggesting they are far-field signals decaying as $1/r$. On the other hand, long-period signals at distances within 5 km decay much more rapidly, indicating that they are the FSD. This is the nature of the signals analyzed in the present paper.

station to station are also taken into account in the inversion via Green's functions, the large uncertainty on the difference of travel time at low frequency does not give a good constraint on the location. The good constraint of location is partly attributed to the rapid variation of amplitudes of the FSDs.

When FSD dominates at near-field stations, waveforms are similar on the three components of a same station. Hence the polarization is linear, pointing to the source direction and the signal appears like P-waves. This justifies the usage of polarization to determine the source location (Appendix B; three-component semblance method of Matsubayashi, 1995; Kaneshima et al., 1996; Kawakatsu et al., 2000 – this issue). We should, however, note here that there could be another effect that may destroy the linearity in the polarization to some extent. When the source has a finite size and when the stations are very close to the source, polarization will become non-linear. At Aso, this appears to be the case for two stations (UMN and THG); therefore, these two stations are not used in the study of polarization for which a point source is assumed. The effect of a finite source will be discussed in future work.

4.2. The source mechanism

The best solution for LPTs and phreatic eruptions and errors of each component of the moment tensors are listed in Table 1. The error of each component is estimated by the standard deviation of the distribution of the component of all the solutions. Focal mechanisms of LPTs at 15 s and phreatic eruptions are very similar (cf. Appendix A). The similarity of locations and focal mechanisms of all solutions suggests that both LPTs and phreatic eruptions are manifestations of similar physical processes originating from similar locations. Kaneshima et al. (1996) interpreted this as the pressurization and de-pressurization of a hydrothermal reservoir located beneath the active crater.

Interpretation of the very small deviatoric components of the moment tensor (~10%) at this point requires caution. Best constrained are the eigenvectors associated with the greatest absolute value of the deviatoric component; these correspond to the *P*-axis for LPTs and phreatic eruptions at 15 s and *T*-axis for LPTs at 7.5 s in Fig. A1. For the first two groups, the largest eigenvalue dominates the solution, and the other two eigenvalues have similar values in

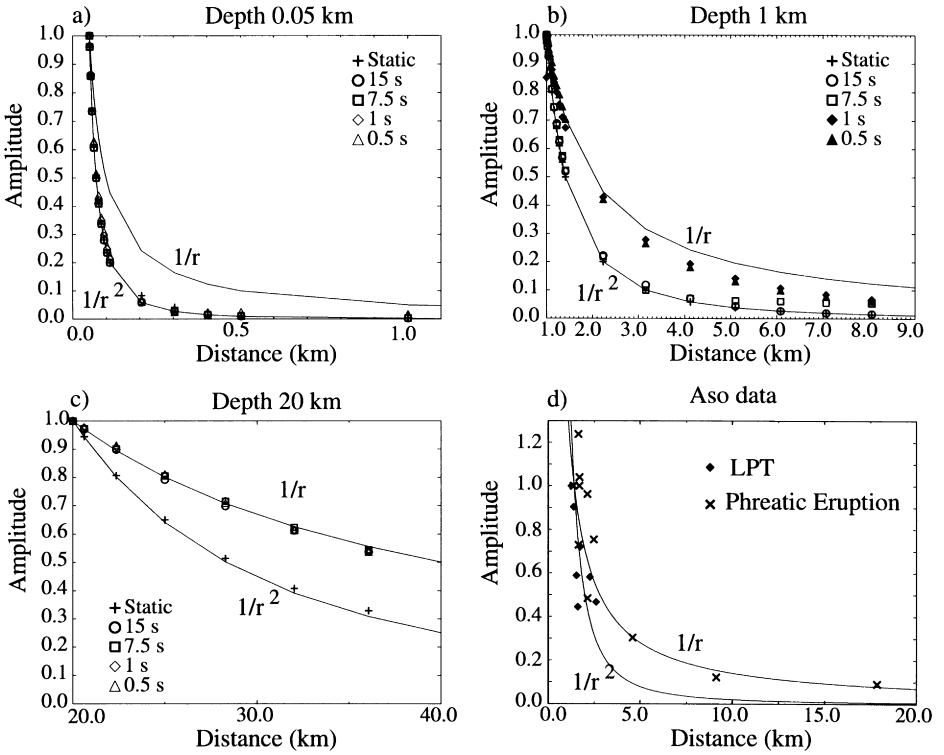

Fig. 10. Amplitude of the filtered signals at 15, 7.5, 1 and 0.5 s as a function of distance. The distance here is defined as the total distance of the receiver from the source, and not the horizontal (epicentral) distance. The amplitudes of the static displacement are also shown. (a) Focal depth of 0.05 km: all the filtered signals decay as $1/r^2$. (b) Focal depth of 1 km: only the static and the 15 and 7.5 s filtered signals decay as $1/r^2$. (c) Focal depth of 20 km: only the static displacement decays as $1/r^2$. At all other frequencies, the decay is as $1/r$. (d) Real data at Aso filtered at 15 s (diamonds are for an LPT, crosses are for a phreatic eruption). For each event, the amplitude is normalized by the value at about a distance of 1.4 km. For large distances, the observed amplitudes decay as $1/r$, whereas for short distances, they seem to decay as fast as $1/r^2$.

magnitude (Table 1). In this case it is natural to decompose the moment tensor into opening crack and isotropic components with common principal axes (e.g. Foulger and Long, 1984); i.e. $\mathbf{M} \approx \alpha \times Iso + \beta \times Crack$, where Iso is the unit isotropic part whose eigenvalues are (1:1:1) (different from the isotropic part $\mathbf{I}$ defined previously) and Crack is a unit opening *crack* part whose eigenvalues are (1:3:1) for a Poisson material. From Table 1, we find $\alpha \sim -2.41 \times 10^{11}$ N m and $\beta \sim -0.68 \times 10^{11}$ N m for the best LPT solution at 15 s. This suggests that the source of LPT and phreatic eruption may be represented as a combination of isotropic and crack parts with the ratio of 3.6:1. This decomposition into vertical opening crack and isotropic parts is consistent with the suggestion of Kaneshima et al. (1996); however we need more extensive spatial coverage of broadband stations to confirm its validity.

5. Conclusion

We present a method to invert and locate LPTs and phreatic eruptions recorded at low frequencies in the near-field at Aso Volcano. We show that the good accuracy of location (a few hundred meters) at long periods (15 and 7.5 s) is related to the use of the long-period (15, 7.5 s) FSD. All the LPTs and phreatic eruptions show similar focal mechanisms and similar locations, confined in a narrow region of a few hundred meters, between 1.1 and 1.5 km below the first crater. This suggests a common origin for the low-frequency part of the signal of all the events studied. Focal mechanisms are mainly isotropic, with a small deviatoric component. This isotropic component may be interpreted as a combination of an opening crack plus an additional isotropic part.

A simple notion that the location of a seismic event cannot have a precision better than the wavelength of the waves is not obvious in the case of near-field. Our long-period data used for the inversion consists mainly of the FSD, whose amplitude is proportional to the source time function. The FSD decays as $1/r^2$, more rapidly than the far-field waves, enabling us to constrain the source location within the precision of a small fraction (a few hundreds meters) of the wavelength (~20 km).

Using a combination of the closest broadband stations and those at the remote sites successfully discriminates the isotropic and vertical CLVD components, as synthetic seismograms for the two models are oppositely polarized at these sets of stations. We have shown that the isotropic model fits the Aso data well, whereas a vertical CLVD cannot, especially for the second set of stations.

In the near-field, to constrain the location and source mechanism well, it is important to have stations at a variety of distances and azimuths. Stations close to the source are especially important to record the rapid decay of FSD.

Acknowledgements

H.K. and D.L. thank the Inoue Foundation for financial support (1995–1997) through the Inoue Fellowship. We thank an anonymous reviewer for carefully reading and commenting on the manuscript.

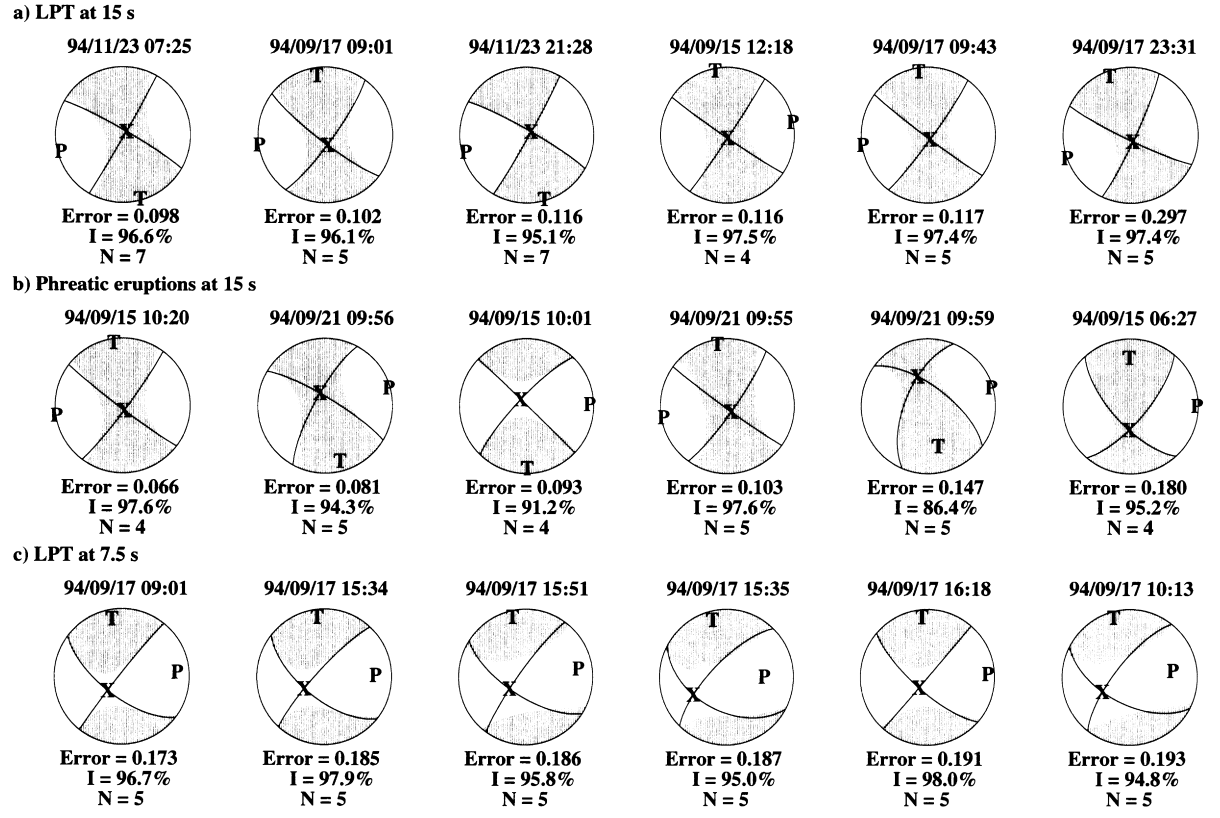

Fig. A1. The deviatoric parts of the moment tensors are shown in a lower hemisphere, equal area (Schmidt) projections: (a) LPTs filtered at 15 s; (b) Phreatic eruptions filtered at 15 s; and (c) LPTs filtered at 7.5 s. Event identification are indicated by the above mechanisms, and the RMS error percentage of the isotropic component and the number of stations used are indicated below.

Appendix A. Best focal mechanisms

Examples of the best focal mechanisms are shown. The isotropic component is written as a percentage of the total seismic moment tensor as defined by Silver and Jordan (1982). They define the isotropic scalar seismic moment as: $M_0^I = 1/\sqrt{6}\mathrm{tr}[\mathbf{M}]$ and the deviatoric scalar seismic moment (Fig. A1) as: $M_0^D = \sqrt{1/2\sum_{i=1}^{3}|\lambda_i^D|^2}$, where λ_i^D are the eigenvalues of the deviatoric seismic moment tensor. They also define the isotropic percentage with respect to the total seismic moment tensor as $[M_0^I]^2/[M_0^M]^2$, where $M_0^M = \sqrt{1/2\sum_{i=1}^{3}|\lambda_i^M|^2}$ is the total scalar seismic moment and λ_i^M is the eigenvalue of the total seismic moment tensor **M**. It can be shown that $[M_0^M]^2 = [M_0^I]^2 + [M_0^D]^2$ (Silver and Jordan, 1982).

Appendix B. Location from polarization

As shown in the discussion, in the near-field, we mainly record the FSD which is linearly polarized pointing to the source (like P-waves). So the polarization can be used to locate LPTs and phreatic eruptions.

A non-linear polarization filter (Flinn, 1965) is applied to the data filtered around the first two peaks of the spectrum (15 and 7.5 s of period) for LPTs of 17 September 1994. The polarizations of stations KHE, SUN, TAK and AWS at 15 and 7.5 s are mostly rectilinear. On the other hand, the polarizations at stations UMN and THG are not rectilinear and these stations are not used in the analysis. The direction of the main polarization are plotted on a 3D diagram, a projection in the horizontal plane and two vertical planes (Fig. B1). The directions of polarization may not cross in 3D, nevertheless projections in a horizontal plane and two vertical planes as shown in Fig. B1 give a rough idea of the locations, which are similar to the ones found by the 3D grid method. The solutions given by the polarization analysis for the periods of 15 and 7.5 s are (0.3 km south, 0.1 km west, 1.1 km depth) and (0.1 km south, 0.1 km west, 1.1 km depth), respectively. The origin of the coordinate system is again the center of the active crater. The error of location with the polarization is bigger than that with the inversion, and is estimated to be about 500 m horizontally and about 800 m vertically based on Fig. B1.

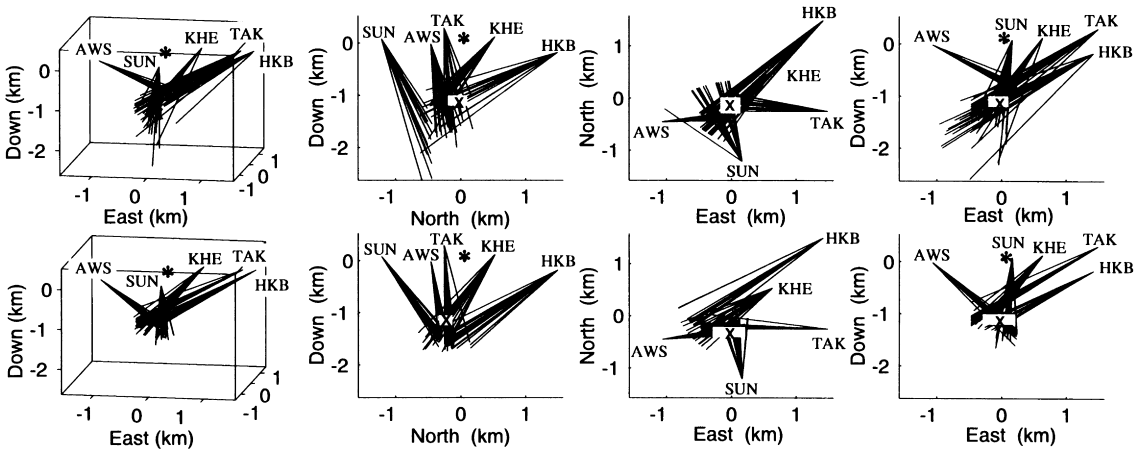

Fig. B1. Directions of polarization for different LPTs of 17 September 1994. Top: for data filtered around 7.5 s. Bottom: for data filtered around 15 s. The cross gives the location of highest density of the directions in 3D. The star corresponds to the first crater. Altitude corrections are included. A 3D diagram and a projection in the horizontal plane and two vertical planes are shown. Note that apparently converging directions of polarization in 2D projections are shown to be non-intersecting in 3D; hence, interpretation of event locations made from projections may be misleading.

References

Aki, K., Richards, P.G., 1980. Quantitative Seismology, Theory and Methods. W.H. Freeman, San Francisco, CA.

Chouet, B.A., 1996. New methods and future trends in seismological volcano monitoring. In: Scarpa, R., Tilling, R.I. (Eds.), Monitoring and Mitigation of Volcano Hazards. Springer, Berlin, pp. 23–97.

Flinn, E., 1965. Signal analysis using rectilinearity and direction of particle motion. Proc. IEEE 53, 1874–1876.

Foulger, G., Long, R.E., 1984. Anomalous focal mechanisms: tensile crack formation on an accreting plate boundary. Nature 310, 43–45.

Frémont, M., Malone, S.D., 1987. High precision relative locations of earthquakes at Mount St. Helens, Washington. J. Geophys. Res. 92, 10 223–10 236.

Johnson, L.R., 1974. Green's function for Lamb's problem. Geophys. J. R. Astron. Soc. 37, 99–131.

Julian, B., Foulger, G., 1996. Earthquake mechanisms from linear-programming inversion of seismic-wave amplitude ratios. Bull. Seismol. Sos. Am. 86, 972–980.

Julian, B., Sipkin, S., 1985. Earthquake processes in the Long Valley Caldera area, California. J. Geophys. Res. 90, 11 155–11 169.

Kanamori, H., Given, J.W., 1981. Use of long period surface waves for rapid determination of earthquake source parameters. Phys. Earth Planet. Inter. 27, 8–31.

Kanamori, H., Given, J.W., 1982. Analysis of long period seismic waves excited by the May 18, eruption of Mount St. Helens: a terrestrial monopole?. J. Geophys. Res. 87, 5422–5432.

Kaneshima, S., Kawakatsu, H., Matsubayashi, H., Sudo, Y., Tsutsui, T., Ohminato, T., Ito, H., Uhira, K., Yamasato, H., Oikawa, J., Takeo, M., Iidaka, T., 1996. Mechanism of phreatic eruptions at Aso Volcano inferred from near-field broadband seismic observations. Science 273, 642–645.

Kawakatsu, H., 1996. On the observability of the isotropic component of a moment tensor. Geophys. J. Int. 126, 525–544.

Kawakatsu, H., Ohminato, T., Ito, H., Kuwahara, Y., Kato, T., Tsuruga, K., Honda, S., Yomogida, K., 1992. Broadband seismic observation at the Sakurajima Volcano, Japan. Geophys. Res. Lett. 19, 1959–1962.

Kawakatsu, H., Ohminato, T., Ito, H., 1994. 10 s-Period volcanic tremors observed over a wide area in southwestern Japan. Geophys. Res. Lett. 21, 1963–1966.

Kawakatsu, H., Kaneshima, S., Matsubayashi, H., Ohminato, T., Sudo, Y., Tsutsui, T., Uhira, K., Yamasato, H., Ito, H., Legrand, D., 2000. Aso94: Aso seismic observation with broadband instruments. J. Volcanol. Geotherm. Res. 101, 129–154.

Knopoff, L., Randall, M., 1970. The compensated linear vector dipole: a possible mechanism for deep earthquakes. J. Geophys. Res. 75, 4957–4963.

Legrand, D., 1995. Study of a population of tectonic and volcanic earthquakes in near field: from classical seismology to non linear effects. PhD thesis, Institut de Physique du Globe de Strasbourg (in French).

Lesage, Ph., Surono, 1995. Seismic precursors of the February 10, 1990 eruption of Kelut Volcano, Java. J. Volcanol. Geotherm. Res., 135–146.

Matsubayashi, H., 1995. Origin of the long-period tremors and long-period seismic waves preceding mud-eruptions observed at Aso volcano. Master's thesis, University of Tokyo (in Japanese).

Mogi, K., 1958. Relations between the eruptions of various volcanoes and the deformations of the ground surfaces around them. Bull. Earthquake Res. Inst. 36, 99–134.

Neuberg, J., Lucket, R., Ripepe, M., Braun, T., 1994. Highlights from a seismic broadband array on Stromboli volcano. Geophys. Res. Lett. 21, 749–752.

Ohminato, T., Ereditato, D., 1997. Broadband seismic observations at Satsuma-Iwojima volcano, Japan. Geophys. Res. Lett. 24, 2845–2848.

Ohminato, T., Chouet, B., Dawson, P., Kedar, S., 1998. Waveform inversion of very long period impulsive signals associated with magmatic injection beneath Kilauea volcano, Hawaii. J. Geophys. Res. 103, 23 839–23 862.

Poupinet, G., Glangeaud, F., Cote, P., 1982. P-time delay measurements of doublets of microearthquakes. Proc. IEEE ICASSP82, 1516–1519.

Rowe, C.A., Aster, R.C., Kyle, P.R., Schlue, J.W., Dibble, R.R., 1998. Broadband recording of Strombolian explosions and associated very-long-period seismic signals on Mount Erebus volcano, Ross Island, Antarctica. Geophys. Res. Lett. 25, 2297–2300.

Sassa, K., 1935. Volcanic micro-tremors and eruption-earthquakes. Mem. Coll. Sci. Kyoto Univ., Series A 18, 255–293 (Part 1 of the geophysical studies on the volcano Aso).

Silver, P., Jordan, T., 1982. Optimal estimation of scalar seismic moment. Geophys. J. R. Astron. Soc. 70, 755–787.

Uhira, K., Takeo, M., 1994. The source of explosive eruptions of Sakurajima volcano, Japan. J. Geophys. Res. 99 (B9), 17 775–17 789.